Quantum process tomography on vibrational states of atoms in an optical lattice

S. H. Myrskog, J. K. Fox, M. W. Mitchell, and A. M. Steinberg
Department of Physics, University of Toronto, 60 St. George Street, Toronto, Ontario, Canada M5S 1A7
(Received 4 April 2005; published 25 July 2005)

Quantum process tomography is used to fully characterize the evolution of the quantum vibrational state of atoms. Rubidium atoms are trapped in a shallow optical lattice supporting only two vibrational states, which we characterize by reconstructing the 2×2 density matrix. Repeating this reconstruction for a complete set of inputs allows us to completely characterize both the system's intrinsic decoherence and resonant coupling.

DOI: 10.1103/PhysRevA.72.013615 PACS number(s): 03.75.Be, 03.75.Gg

In recent years, there have been remarkable advances in directly controlling and observing the dynamics of individual quantum systems in a variety of domains. This degree of control of microscopic systems is one of the technological advances underlying the myriad proposals for realistic quantum-information processing systems. For instance, a number of quantum-computing proposals rely on atoms trapped in an optical lattice [1,2], a system in which a great deal of work has investigated coherent center-of-mass motion [3–5], full characterization of spin states [6], quantum state reconstruction of trapped ions and atoms [7–9], loading of individual atoms into lattice sites [10], and coherent interactions between atoms [11–13]. Here we demonstrate a technique for completely reconstructing the quantum state of motion of atoms trapped in an optical lattice. By performing this density-matrix reconstruction for a complete set of input states, we are able to completely characterize the quantum evolution of the system (the "superoperator"), including decoherence.

Such characterization will be necessary in order to implement quantum error correction [14]; the development of a quantum computer will require reducing errors to below a certain threshold [15]. An arbitrary operation may be characterized using quantum process tomography (QPT) [16]. The result of QPT is the superoperator, a positive, linear map from density matrices to density matrices, which governs the evolution of the density matrix for the operation. Unlike a propagator, the superoperator allows for nonunitary evolution of the system, thoroughly characterizing decoherence, relaxation, and loss in a system. From the superoperator one can determine which errors occur and develop procedures to reduce or eliminate them, without prior assumptions about the underlying physical mechanisms [17].

QPT has recently been demonstrated using spins in a NMR system [18], the polarization of single photons [19] and photon pairs [20], and an optical controlled-NOT gate [21]. QPT is performed by preparing a complete set of input density matrices, subjecting each to the operation being tested, and measuring the resultant output density matrices. Due to the linearity of quantum mechanics, QPT of a process on an N-dimensional system requires $O(N^2)$ linearly independent input density matrices. Alternatively, it has recently been shown that one can use a single state in a larger Hilbert space as the input [19,22,23].

We perform quantum process tomography using the motional states of atoms trapped in the potential wells of a one-dimensional (1D) optical lattice. We examine processes that involve only the motional states of the atoms, not their electronic state. The measurements are insensitive to the long-range degrees of freedom and effectively trace over the quasimomentum in the Bloch state picture (or equivalently the well index in the Wannier state picture). We use a shallow 1D lattice which supports only two bound bands, which we label as ground ($|0\rangle$) and excited ($|1\rangle$). The lattice is vertically oriented, causing all atoms in higher-energy, classically unbound states to quickly fall out of the lattice and become spatially separated from the bound states (the Landau-Zener tunneling rates from the three lowest-energy bands are 3×10^{-7}, 14.5, and 1150 s^{-1} in increasing order). A typical sequence, from state preparation in the lattice to measurement, lasts 20 ms.

We cool and trap ^{85}Rb atoms in a standard vapor cell magneto-optical trap MOT to a temperature of 7 μK with a rms radius of approximately 1 mm. The optical lattice is applied during a post-trapping optical molasses phase. The optical lattice is created by interfering two laser beams which are detuned 30 GHz below the Rb $D2$ resonance at 780.03 nm. The relative phase of the beams, and thus the displacement of the lattice, is controlled via acousto-optic modulators that are driven by a common source. The beams are superposed with orthogonal polarizations using a polarizing beam splitter. The beams copropagate to the vacuum system, passing through a spatial filter to mode-match the beams, ensuring that fringes forming the lattice are flat and horizontal. The beams are separated with another polarizing beam splitter just before they enter the vacuum chamber. The lattice beams have an angle of 50° between them, in a vertical plane, creating a vertically oriented optical lattice with a lattice constant of $L=0.93$ μm. The depth of the lattice is controlled by the intensity and detuning of the beams, and is chosen to be $E_0=18E_r$ (where $E_r=h^2/8L^2m=h\times 690$ Hz is the effective recoil energy of the lattice, h is Planck's constant, and m is the mass of the Rb atom) at which depth it contains two bound states. The energy separation between the states is $h\times 5.0$ kHz and the scattering rate is on the order of 4 Hz, which is insignificant on the time scale of the experiment.

We measure the populations of the $|0\rangle$ and $|1\rangle$ bands by adiabatically releasing the atoms from the lattice; as the depth of the lattice is adiabatically decreased, the energy bands approach the top of the potential. Once an energy band

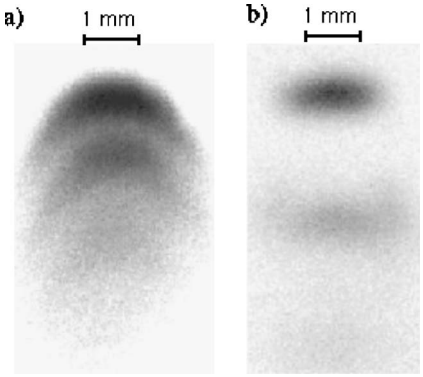

FIG. 1. (a) A fluorescence image of the state populations in a lattice obtained by continuous adiabatic decrease of the lattice potential over a period of 45 ms. An adiabatic stepwise decrease of the potential leads to a clearer separation of the states as shown in (b).

becomes classically unbound, the atoms in that band accelerate downward due to gravity. Since each band becomes unbound at a different time, each is mapped to a different vertical position. The spatial distribution is recorded by fluorescence imaging. Alternatively, the lattice depth may be quickly, but still adiabatically, lowered to a depth of $9E_r$. At this depth the ground state has a Landau-Zener-limited lifetime of 250 ms while the excited state has a lifetime of 0.5 ms; the latter quickly escape the lattice while the former remain trapped. After holding the depth constant for some time (typically for about 20 ms), the relative populations can be determined as shown in Fig. 1(b). In order to satisfy the adiabatic criterion we must decrease the potential slower than $dE_0/dt \ll h \times 10^8/\mathrm{s}^2$; the fastest decrease we use is $dE_0/dt = h \times 4.1 \times 10^6/\mathrm{s}^2$, and we observed nonadiabatic effects only with a turn-off faster than $dE_0/dt \approx h \times 1.4 \times 10^7/\mathrm{s}^2$. The lattice beams have a Gaussian shape with rms width of 3 mm, creating a shallower lattice near the edges. The correspondingly earlier release times at the edges result in the curved clouds seen in Fig. 1(a). To reduce broadening from inhomogeneous well depths we collect signal only from the central 600 μm of the cloud.

A sample of ground-state atoms is prepared by filtering out the excited-state atoms from the lattice. We hold the well depth near $9E_r$ for about 3 ms, allowing most atoms in $|1\rangle$ to escape. The depth is then adiabatically increased back to the original depth, preparing a sample of atoms with up to 95% occupation of the ground state. To prepare a variety of initial states, we make use of our ability to displace the lattice, and of the atoms' free evolution. Displacement of the lattice is equivalent to a spatial translation of the atom cloud in the lattice's reference frame, constituting a coherent coupling between the energy eigenstates. In addition to coupling the two bound states, this induces some transitions to unbound states, which are lost from the lattice. Spatial translations change the coefficients of the states as described by the following equations:

$$|0\rangle \overset{\Delta x}{\Rightarrow} c_{00}|0\rangle + c_{10}|1\rangle + (\text{loss}), \tag{1}$$

$$|1\rangle \overset{\Delta x}{\Rightarrow} -c_{10}^{*}|0\rangle + c_{11}|1\rangle + (\text{loss}). \tag{2}$$

The coefficients c_{00}, c_{10}, and c_{11} are determined by displacing the lattice with different initial state populations. The "loss" term represents coupling of atoms to unbound states of the lattice. For a displacement $\Delta x = L/8 = 116$ nm we measure c_{00}, c_{10}, and c_{11} to be 0.86(2), 0.50(2), and 0.53(10), respectively, close to the theoretical values of 0.87, 0.45, and 0.63. During a time period Δt of free evolution in the lattice, the ground and excited states acquire a relative phase shift of $\omega \Delta t$, where ω is the oscillation frequency in the lattice. Using a combination of displacement and time delay we can prepare superposition states with arbitrary relative phase.

State tomography [24,25] is performed by projecting the unknown state onto a set of known states. We use a set of nonorthogonal states $\{\Phi_1, \ldots, \Phi_4\} = \{|0\rangle, |1\rangle, |\theta_x\rangle, |\theta_y\rangle\}$ where $|\theta_x\rangle = \cos\theta|0\rangle + \sin\theta|1\rangle$ and $|\theta_y\rangle = \cos\theta|0\rangle + i\sin\theta|1\rangle$. We project onto states of the form $\cos\theta|0\rangle + \sin\theta|1\rangle$ by spatially displacing the trapping potential before separating the resulting energy eigenstates. We choose our displacements to be small in order to have negligible coupling to the higher-energy, unbound states; at $\Delta x = 116$ nm we measure $\theta \approx 0.5$ rad. Projection onto the state $|\theta_y\rangle$ is accomplished by adding a quarter-period time delay prior to displacement of the trapping potential. State tomography is performed by measuring the projections $m_i = \langle \Phi_i|\rho|\Phi_i\rangle$ for all states $|\Phi_i\rangle$. The resulting measurements $\{m_1, \ldots, m_4\}$ are used to reconstruct the density matrix, with $\rho_{11} = m_1$, $\rho_{22} = m_2$, and $\rho_{12} = [(m^3 + im^4) - m_1 \cos^2\theta - m_2 \sin^2\theta]/\sin 2\theta$.

We perform QPT of the "process" of free evolution within the lattice, to fully characterize the decoherence. We prepare and characterize a known state, allow it to evolve for 200 μs (one oscillation period), and measure the resulting density matrix by state tomography as above. Repeating this with four linearly independent input states allows reconstruction of the process. The four states we use are the ground state ρ_g, prepared as above; a superposition of $|0\rangle$ and $|1\rangle$ with real coherence ρ_r, prepared by displacing the ground state; a superposition with imaginary coherence ρ_i, prepared by adding a quarter-period delay after displacement; and a mixed state ρ_m. The mixed state can be prepared by either omitting the filtering step, or preparing a superposition state and waiting 3 ms for it to decohere (see discussion below). Table I shows the projection of each input density matrix onto the states $\{\Phi_1, \ldots, \Phi_4\}$, before (left) and after (right) the "operation." The same data are displayed graphically in Fig. 2. Note the decreased contrast in the projections of ρ_r and ρ_i onto $|\Phi_3\rangle$ and $|\Phi_4\rangle$, as expected for an operation where the coherence of the state decreases.

The superoperator $\mathcal{E}$ resulting from QPT can be expressed in a number of ways. One common form is the operator sum representation,

$$\rho_{out} = \mathcal{E}(\rho_{in}) = \sum_i \hat{A}_i \rho_{in} \hat{A}_i^{\dagger}, \tag{3}$$

where $\hat{A}_i$ are operational elements, often called Kraus operators [26], subject to the constraint $\Sigma_i \hat{A}_i^{\dagger}\hat{A}_i = I$. The Choi matrix [27,28] provides a straightforward procedure to obtain

TABLE I. Projection of the prepared states onto the measurement state. The table on the left shows the projections after state preparation, and the table on the right shows the projections after one period of free evolution.

	ρ_g	ρ_m	ρ_r	ρ_i		ρ_g	ρ_m	ρ_r	ρ_i
$\|0\rangle$	0.90	0.60	0.69	0.69	$\|0\rangle$	0.90	0.60	0.69	0.69
$\|1\rangle$	0.10	0.40	0.31	0.31	$\|1\rangle$	0.10	0.40	0.31	0.31
$\|\Phi_x\rangle$	0.82	0.59	0.85	0.63	$\|\Phi_x\rangle$	0.83	0.60	0.82	0.65
$\|\Phi_y\rangle$	0.84	0.58	0.64	0.37	$\|\Phi_y\rangle$	0.82	0.57	0.70	0.46

experimental Kraus operators. The Choi matrix is defined as $\underline{C}=\Sigma_{i,j}|i\rangle\langle j|\otimes\mathcal{E}(|i\rangle\langle j|)$ where $|i\rangle\langle j|$ is an outer product of basis states and $\mathcal{E}(|i\rangle\langle j|)$ is the superoperator acting on the matrix given by the outer product $|i\rangle\langle j|$. Then $\mathcal{E}(\rho)=\Sigma_{i,j}C_{i,j}\rho_{i,j}$ where $C_{i,j}=\mathcal{E}(|i\rangle\langle j|)$ is the (i,j)th 2×2 submatrix of $\underline{C}$ and $\rho_{i,j}$ is the (i,j)th element of the density matrix. The eigenvalues and eigenvectors of $\underline{C}$ can then be used to determine the canonical Kraus operators, given by $\hat{A}_i=\sqrt{\kappa_i}\hat{k}_i$, where κ_i is the ith eigenvalue and $\hat{k}_i$ is the corresponding eigenvector written in matrix form. Using a maximum-likelihood technique, we find the Choi matrix that best predicts the measured output states given the measured input states. As we may lose atoms from the system under some operations we do not enforce the Choi matrix to preserve the trace of the density matrix; however, we do limit the search to physical, i.e., completely positive, Choi matrices. If the system does exhibit loss then the measured matrix is the projection of the full Choi matrix, including higher-energy levels, onto the two lowest-energy states. We find the Choi matrix to be

$$\underline{C}=\begin{bmatrix} 0.99 & -0.01i & 0.00 & 0.64-0.03i \\ 0.01i & 0.01 & 0.00 & 0.00 \\ 0.00 & 0.00 & 0.04 & 0.05-0.04i \\ 0.64+0.03i & 0.00 & 0.05+0.04i & 0.98 \end{bmatrix}, \tag{4}$$

with uncertainties, equal for real and imaginary components (when present), of 0.12 for the off-diagonal corners, 0.08 for the 3,4 and 4,3 elements, and $\leqslant 0.04$ for the rest. The Choi matrix for the process of free evolution preserves the trace of the density matrix, with the constraint $\Sigma_i\hat{A}_i^\dagger\hat{A}_i=I$ having deviations no larger than 0.02. The Choi matrix after one oscillation in the lattice is dominated by the corner elements, which map elements of the density matrix onto themselves. The diagonal corners represent the mapping of populations into populations, and show that the state populations are nearly unchanged. The off-diagonal corners, which map coherences into coherences, are significantly less than 1, showing a 36% loss of coherence. The most significant Kraus operators are found to be $\hat{A}_1=0.90\hat{I}+\hat{R}_1$ and $\hat{A}_2=-0.41\hat{\sigma}_z+\hat{R}_2$ where $\hat{I}$ is the identity, $\hat{\sigma}_z$ is a Pauli matrix, and $\hat{R}_1,\hat{R}_2$ are small remainders with magnitudes bound by $\mathrm{Tr}[\hat{R}_i^\dagger\hat{R}_i]\leqslant 0.03$. The other two Kraus operators are insignificant on the scale of our experimental resolution, also satisfying a similar bound. Kraus operators of the form $\hat{I}$ and $\hat{\sigma}_z$ are consistent with pure dephasing, as expected for either interwell tunneling or inhomogeneous broadening.

The same data may be visually displayed using a Bloch sphere representation [19,29], which has the advantage of showing how any state on the surface of the Bloch sphere evolves into a new state. Figure 3(a) shows the initial, undisturbed Bloch sphere before evolution in the lattice, and Fig.

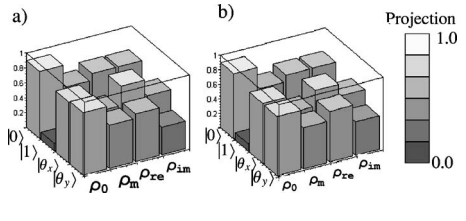

FIG. 2. Matrix of measured projections. Input density matrices (reading left to right: ground state, mixed state, superposition with real coherence, and superposition with imaginary coherence) are shown along the bottom while the postselected states are listed on the side. Note the decreased contrast in the θ_x and θ_y projections for the superposition states. All populations are unchanged to within experimental error.

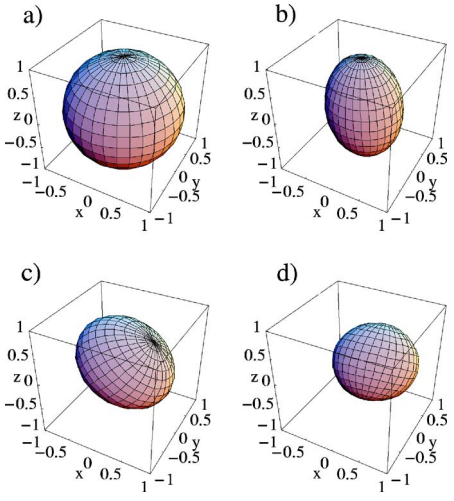

FIG. 3. Bloch sphere representation of process tomography. (a) The initial Bloch sphere representing the space of pure input states. (b) After one period of free evolution the sphere contracts horizontally due to a loss of coherence. (c) After sine drive showing rotation about the y axis. (d) After cosine drive, showing rotation about the x axis.

3(b) shows the Bloch sphere after one oscillation. The sphere becomes prolate, contracting toward the z axis by 36%, as expected. The coherence time is thus found to be 540 ± 60 μs (2.8 ± 0.3 periods), much shorter than the expected coherence time of 2 ms based on the width of the excited band (the interwell tunneling rate). The number of oscillations is, however, consistent with oscillations observed in other work [4,30,31]. It is believed that the observed decoherence is actually dominated by dephasing caused by inhomogeneity in the lattice beams, including their 3 mm Gaussian width and possibly smaller-scale fringes. The addition of antireflection-coated slides to the vacuum cell did not change the observed coherence time. Using a pulse-echo style experiment, we have observed revivals that decay with a time constant of 0.8 ms [32]. Unlike earlier experiments, we use a two-level system, and anharmonicity is therefore not a factor in the observed decoherence.

An example of an operation necessary for quantum-information processing is a single-qubit rotation. To demonstrate the applicability of process tomography to characterizing such operations we attempt to perform a rotation of the Bloch sphere by a method equivalent to a Rabi oscillation. We sinusoidally drive the displacement of the lattice at the trap frequency, thereby coupling neighboring states coherently. Process tomography is performed after a single period of this drive. The displacement is kept small to ensure that coupling is predominantly between neighboring states. We test both a sine drive $\Delta x(t)=x_m \sin(\omega_0 t)$ and a cosine drive $\Delta x(t)=x_m[\cos(\omega_0 t)-1]$, where $x_m=26$ nm is the displacement and ω_0 is the oscillation frequency in the lattice and the pulse lasts from $t=0$ to $t=2\pi/\omega_0$. We again find the Choi matrix from a maximum-likelihood model, but find the Bloch sphere representation to be the most intuitive. For these coupling operations we do observe some loss from the system, but the loss does not exceed 20%. As we do observe loss with the sine and cosine drives, the results of the measurements give the projection of the full Choi matrix onto the lowest two states of the system. The superoperator for the sine drive is found to be

$$C_{sin}=\begin{bmatrix} 0.91 & -0.22+0.07i & 0.26-0.06i & 0.42-0.33I \\ -0.22-0.07i & 0.10 & -0.06+0.02i & -0.10+0.11i \\ 0.26+0.06i & -0.06-0.02i & 0.22 & 0.19-0.06i \\ 0.42+0.33I & -0.10-0.11i & 0.19+0.06i & 0.53 \end{bmatrix}. \tag{5}$$

For a cosine drive we find

$$C_{cos}=\begin{bmatrix} 0.86 & 0.14-0.25i & -0.25i & 0.50-0.09i \\ 0.14+0.25i & 0.16 & 0.08-0.01i & 0.03+0.13i \\ 0.25i & 0.08+0.01i & 0.13 & 0.03+0.17i \\ 0.50+0.04i & 0.03-0.13i & 0.03-0.17i & 0.51 \end{bmatrix}. \tag{6}$$

Qualitative information about the the process can be more easily determined from a Bloch sphere representation. As a Bloch sphere does not accurately represent non-normalized states, we first normalize the measured density matrices before determining the Choi matrix. Figures 3(c) and 3(d) show the resulting normalized Bloch spheres, which have rotations of 35.5° and 36.4° about the y and x axis, respectively. The Bloch spheres are rotated about orthogonal axes, as expected for driving fields 90° out of phase. The resulting shape is again a spheroid, but the radius has decreased in all dimensions. In particular, the length of the semiminor axis for the sinusoidal drive is 0.69 (while it should be noted that in the absence of the coherent drive, it decayed to a value of 0.64). A simulation using a truncated harmonic-oscillator model predicts a rotation of 35.0° about the y axis.

We have presented a technique for determining the motional quantum state of atoms in an optical lattice. Using displacements, delays, and adiabatic relase of atoms from the lattice we make projective measurements onto several superposition states, as needed for quantum state tomography. We have performed quantum process tomography on three elementary operations for quantum-information processing: free evolution and two different single-qubit rotations. We have extracted the superoperators describing the intrinsic dephasing of the system over time and the effectiveness of single-qubit rotations induced by resonant modulation of the lattice position. We plan to extend these techniques to test the Markovian approximation; to characterize and optimize bang-bang methods [33,34] for removing inhomogeneous-broadening effects; and to study the well-depth dependence of the decoherence, investigating the role of interwell tunneling, Wannier-Stark transitions, and Bloch oscillations. Process tomography allows the tailoring of error correction protocols to the observed behavior of particular physical realizations of quantum-information systems [35,36]. This system-by-system tailoring will likely prove essential if error thresholds on the order of 10^{-4} or 10^{-5} are ever to be reached [15]. More generally, it is the only method to permit complete characterization of the evolution of open quantum systems, and should play a central role in the toolbox for control

and study of individual quantum systems, whether for quantum-information processing or for other applications.

We thank Daniel Lidar and Samansa Maneshi for helpful discussions, and Sara Schneider for assistance with the maximum-likelihood methods. This work was supported by the DARPA-QuIST program (managed by AFOSR under Agreement No. F49620-01-1-0468), the National Science and Engineering Research Council of Canada, the Canadian Institute for Photonics Inovation, and eMPOWR.

[1] G. Brennen *et al.*, Phys. Rev. Lett. **82**, 1060 (1999).
[2] D. Jaksch *et al.*, Phys. Rev. Lett. **82**, 1975 (1999).
[3] F. Buchkremer *et al.*, Phys. Rev. Lett. **85**, 3121 (2000).
[4] B. K. Teo *et al.*, Phys. Rev. Lett. **88**, 173001 (2002).
[5] N. V. Morrow *et al.*, Phys. Rev. Lett. **88**, 093003 (2002).
[6] G. Klose *et al.*, Phys. Rev. Lett. **86**, 4721 (2001).
[7] D. Leibfried *et al.*, Phys. Rev. Lett. **77**, 4281 (1996).
[8] P. Bertet *et al.*, Phys. Rev. Lett. **89**, 200402 (2002).
[9] J. K. Fox, S. Maneshi, S. H. Myrskog, and A. M. Steinberg (unpublished).
[10] S. Peil *et al.*, Phys. Rev. A **67**, 051603(R) (2003); M. Griener *et al.*, Nature (London) **419**, 51 (2002); J. Vala *et al.*, Phys. Rev. A **71**, 032324 (2005).
[11] H. J. Briegel *et al.*, J. Mod. Opt. **47**, 415 (2000).
[12] G. K. Brennen *et al.*, Phys. Rev. A **65**, 022313 (2002).
[13] O. Mandel *et al.*, Nature (London) **425**, 937 (2003).
[14] P. W. Shor, Phys. Rev. A **52**, R2493 (1995); A. Steane, Proc. R. Soc. London, Ser. A **454**, 2551 (1996); P. Zanardi and M. Rasetti, Phys. Rev. Lett. **79**, 3306 (1997); D. A. Lidar *et al.*, *ibid.* **81**, 2594 (1998).
[15] E. Knill *et al.*, Science **279**, 342 (1998); J. Preskill, Proc. R. Soc. London, Ser. A **454**, 385 (1998); D. Gottesman, Phys. Rev. A **57**, 127 (1998); D. Aharonov and M. Ben-Or, in Proceedings of the 29th ACM Symposium on Theory of Computing, 1999 (unpublished), p. 176.
[16] I. L. Chuang and M. A. Nielsen, J. Mod. Opt. **44**, 2455 (1997); J. F. Poyatos *et al.*, Phys. Rev. Lett. **78**, 390 (1997).
[17] E. Knill and R. Laflamme, Phys. Rev. A **55**, 900 (1997).
[18] A. M. Childs *et al.*, Phys. Rev. A **64**, 012314 (2001).
[19] J. B. Altepeter *et al.*, Phys. Rev. Lett. **90**, 193601 (2003).
[20] M. Mitchell *et al.*, Phys. Rev. Lett. **91**, 120402 (2003).
[21] J. L. O'Brien *et al.*, Phys. Rev. Lett. **93**, 080502 (2004).
[22] G. M. D'Ariano and P. LoPresti, Phys. Rev. Lett. **86**, 4195 (2001).
[23] A. Kastberg *et al.*, Phys. Rev. Lett. **74**, 1542 (1995); T. Muller-Sèydlitz *et al.*, *ibid.* **78**, 1038 (1997).
[24] A. Zucchetti *et al.*, Phys. Rev. A **61**, 011405(R) (1999).
[25] R. T. Thew *et al.*, Phys. Rev. A **66**, 012303 (2002).
[26] K. Kraus, *States, Effects and Operations*, (Springer-Verlag, Berlin, 1983).
[27] M. D. Choi, Linear Algebr. Appl. **10**, 285 (1975).
[28] D. Leung, J. Math. Phys. **44**, 528 (2002).
[29] M. A. Nielsen and I. L. Chuang, *Quantum Computation and Quantum Information* (Cambridge University Press, Cambridge, U.K., 2000).
[30] D. L. Haycock *et al.*, Phys. Rev. Lett. **85**, 3365 (2000).
[31] G. Raithel *et al.*, Phys. Rev. Lett. **81**, 3615 (1998).
[32] S. Maneshi, J. K. Fox, M. Partlow, and A. M. Steinberg (unpublished).
[33] L. Viola and S. Lloyd, Phys. Rev. A **58**, 2733 (1998).
[34] L. A. Wu and D. A. Lidar, Phys. Rev. Lett. **88**, 207902 (2002).
[35] M. Pravia *et al.*, J. Phys. Chem. **119**, 9993 (2003).
[36] N. Boulant *et al.*, J. Chem. Phys. **121**, 2955 (2004).